Effects of rattling behavior of K and Cd atoms along different directions in anisotropic KCdAs on lattice thermal transport and thermoelectric properties

Yue Wang,[1] Yinchang Zhao,[1,*] Jun Ni,[2,3] and Zhenhong Dai[1,†]

[1] *Department of Physics, Yantai University, Yantai 264005, People's Republic of China*
[2] *State Key Laboratory of Low-Dimensional Quantum Physics, Department of Physics, Tsinghua University, Beijing 100084, People's Republic of China*
[3] *Frontier Science Center for Quantum Information, Beijing 100084, People's Republic of China*

(Dated: February 6, 2024)

We employ advanced first-principles methodology, merging self-consistent phonon theory and the Boltzmann transport equation, to comprehensively explore the thermal transport and thermoelectric properties of KCdAs. Notably, the study accounts for the impact of quartic anharmonicity on phonon group velocities in the pursuit of lattice thermal conductivity and investigates 3ph and 4ph scattering processes on phonon lifetimes. Through various methodologies, including examining atomic vibrational modes and analyzing 3ph and 4ph scattering processes, the paper unveils microphysical mechanisms contributing to the low κ_L within KCdAs. Key features include significant anisotropy in Cd atoms, pronounced anharmonicity in K atoms, and relative vibrations in non-equivalent As atomic layers. Cd atoms, situated between As layers, exhibit rattling modes and strong lattice anharmonicity, contributing to the observed low κ_L. Remarkably flat bands near the valence band maximum translate into high PF, aligning with ultra-low κ_L for exceptional thermoelectric performance. Under optimal temperature and carrier concentration doping, outstanding ZT values are achieved: 4.25 (a(b)-axis, p-type), 0.90 (c-axis, p-type), 1.78 (a(b)-axis, n-type), and 2.36 (c-axis, n-type).

PACS numbers: 65.40.-b, 66.70.-f, 63.20.-e, 72.20.-i
Keywords: first-principles calculation, anharmonic lattice dynamics, lattice thermal transport, electron transport characteristics, thermoelectric properties, octahedron

I. INTRODUCTION

With the elevation of living standards, there is an escalating demand for material possessions. Among these needs, the energy conundrum has perpetually held a prominent place. As living standards rise, the appetite for energy escalates relentlessly. However, conventional fossil fuels, in addition to being non-renewable, cast a shadow of environmental pollution and climate change. Therefore, the quest for clean and renewable energy alternatives becomes an utmost priority[1, 2]. Enter thermoelectric materials, an emerging domain brimming with latent significance. These materials possess the capability to directly transmute thermal energy into electrical power, a technological feat applicable across a myriad of scenarios, ranging from waste heat recovery to solar cell innovation and the empowerment of passive electronic devices[3, 4]. Researchers are ardently dedicated to the pursuit of highly efficient thermoelectric materials, with the aim of enhancing energy conversion efficiency while concurrently reducing costs. The efficiency of thermoelectric (TE) materials can be quantified through the dimensionless figure of merit, ZT, expressed as $ZT = \frac{S^2\sigma T}{\kappa_L+\kappa_e}$, where S, σ, T, κ_L, and κ_e represent the thermopower, dimensions of electrical conductivity, absolute temperature, lattice thermal conductivity, and electronic thermal conductivity, respectively. From the expression above, achieving a high ZT value necessitates that a material simultaneously possesses a large thermopower (S) and excellent electrical conductivity (σ), while maintaining a low thermal conductivity (κ, where $\kappa = \kappa_L + \kappa_e$). However, there exists a coupling between S and σ, and σ is directly proportional to κ_e, making it challenging to enhance the ZT value by adjusting a single parameter. Consequently, we have devised a strategy involving materials with anisotropic electronic band structures characterized by a large flat region and high dispersion[5–8]. Building upon this foundation, we search for thermoelectric materials with intrinsically low κ_L[9–11]. Furthermore, we can employ various techniques such as strain engineering, doping, introduction of defects, nanostructuring, and alloying to further enhance the ZT value[12–21].

Compounds with ternary phases comprising 2B and 5A group elements of sodium or potassium have consistently garnered extensive attention from the scientific community. The majority of these compounds have been successfully synthesized and are considered highly promising materials for technological applications. These materials, due to their ideal cubic crystal structure and electrical properties, are frequently investigated for photonic applications, such as light-emitting diodes and lasers. However, their comprehensive characterization and development have not yet been fully realized. As an early example, the ternary arsenide KCdAs, featuring potassium, was experimentally synthesized back in 1976[22], yet remarkably little has been reported regarding its thermo-

* y.zhao@ytu.edu.cn
† zhdai@ytu.edu.cn

electric properties. A cohort of exemplary thermoelectric materials hitherto documented, encompassing the likes of PbTe with a ZT of 2.5 at 750 K[23], Rb3AuO boasting a ZT of 3.15 at 800 K[24], SnSe's ZT of 2.6 at 923 K[18], and GeTe's ZT of 2.2 at 740 K[25], coalesce around the cardinal tenet of ultralow κ_L. Nonetheless, prevailing theoretical constructs remain anchored to the ambit of harmonic lattice oscillations, obstinately eschewing the contemplation of ramifications stemming from higher-order anharmonics—an omission incompatible with materials underscored by pervasive anharmonicity.

This paper, driven by advanced first-principles methodology and the amalgamation of self-consistent phonon theory (SCP)[26] and the Boltzmann transport equation (BTE)[27], conducts a comprehensive exploration into the thermal transport and thermoelectric properties of KCdAs. In the quest for lattice thermal conductivity, we meticulously account for the renormalization of phonon group velocities υ, occasioned by the finite-temperature phonon frequencies induced by quartic anharmonicity. Furthermore, we delve into the ramifications of three-phonon (3ph) and four-phonon (4ph) scattering processes on phonon lifetimes (τ). Through the application of various methodologies such as the examination of atomic vibrational modes, phonon spectra, the Güneisen parameter (γ), atomic mean-square displacements, crystal orbital Hamiltonian population analysis, and analyses of three- and four-phonon scattering processes, we unveil the intricate microphysical mechanisms underpinning the low κ_L within KCdAs. Our observations highlight several noteworthy features in KCdAs. Cd atoms manifest significant anisotropy, with the Cd atomic layer sandwiched between As atomic layers, while K atoms stand in isolated isolation outside the Cd-As atomic layers. Remarkably, K atoms exhibit pronounced anharmonicity. Intriguingly, the non-equivalent As atomic layers exhibit relative vibrations, leading to high vibrational frequencies for As atoms. Meanwhile, Cd atoms, nestled between As atomic layers, exhibit rattling modes and display strong lattice anharmonicity, contributing to our ability to capture the low κ_L within KCdAs. Furthermore, in the vicinity of the valence band maximum, we identify remarkably flat bands and favorable dispersion, indicative of superior electronic properties. This translates into high power factors (PF), with the coexistence of ultra-low κ_L and PF perfectly aligning with our quest for exceptional thermoelectric performance. Under optimal temperature and carrier concentration doping in both p-type and n-type regions, we achieve outstanding ZT values, which reach 4.25 (a(b)-axis), 0.90 (c-axis), and 1.78 (a(b)-axis), 2.36 (c-axis).

II. METHODOLOGY

All first-principles calculations are performed based on the projector-augmented wave (PAW)[28] potentials and density functional theory (DFT)[29] to calculate total energy, electronic band structures, ALAMODEE[30] and AMSET[31] package input parameters, and are implemented using the Vienna ab initio simulation package (VASP)[32, 33].

We select a cutoff energy of 500 eV for the plane-wave basis set and employ the Perdew-Burke-Ernzerhof (PBE)[34] functional to treat exchange-correlation interactions. The Brillouin zone is sampled with an **q**-point grid of 10×10×6 centered at the Γ point. Convergence is achieved when the energy convergence criteria are less than 10^{-8} eV and the force convergence criteria are less than 10^{-6} eV/Å. Born effective charges (Z*) and the dielectric tensor, necessary for solving the non-analytic part of the dynamical matrix, are computed using density functional perturbation theory (DFPT)[35]. Subsequently, harmonic (HA) and anharmonic interatomic force constants (IFCs) are computed within a 2×2×1 supercell and a **q**-point grid of 5×5×6. Given the diminishing impact and computational expense of higher-order force constants, we utilize the ALAMODE code to extract force constants from 2nd to 6th order, considering this as encompassing the calculation of all higher-order force constants. In addition, we simulated 20000 steps of ab initio molecular dynamics (AIMD) to estimate the stability of KCdAs at high temperatures, as shown in Supplementary Material Figure. S1[36]. There is no obvious change in free energy, indicating that KCdAs is stable at 700 K.

In essence, we extract second-order force constants from eight random structures generated using the finite-displacement method[37]. Using a Python script, 80 snapshots are captured within the supercell. Subsequently, by applying displacements of 0.2 Å in random directions to each atom in these 80 snapshots, we obtain quasi-random configurations required for first-principles calculations. From these 80 quasi-random configurations, we extract a dataset of forces and displacements. Utilizing the compressed sensing lattice dynamics (CSLD)[38] method, we calculate the required force constants. In this process, we initially fit α= 5.6 × 10^{-7} through cross-validation and then solve for higher-order force constants using the elastic grid method. Temperature-dependent anharmonic phonon energy eigenvalues are computed using SCP theory[26]. This calculation accounts for off-diagonal elements in the phonon self-energy, allowing for the determination of temperature-dependent phonon frequencies. Subsequently, the previously computed Born effective charges and dielectric tensor are used to calculate the non-analytic part of the dynamical matrix. This procedure results in the opening of the transverse optical (TO) and longitudinal optical (LO) branches at the Γ point. Building upon the aforementioned foundations, we harness the advantages of ShengBTE to calculate thermal transport parameters within the FOURPHONON package[39, 40]. We employ a uniform grid of 10×10×6 **q**-points, yielding approximately 3.9×10^5 allowed 3ph processes and 1.3×10^9 allowed 4ph processes. For the solution of 3ph scattering, we utilize an itera-

TABLE I. The static dielectric constantϵ_s, high-frequency dielectric constant ϵ_∞ , Bonn effective charge Z^*, elastic constant C_{ij} (GPa), band gap E_g^{HSE06} (eV) and polar optical phonon frequency ω_{po} (THz) for the KCdAs.

semiconductor	ϵ_s	ϵ_∞	Z^*(As)	Z^*(Cd)	Z^*(K)	C_{11}	C_{12}	C_{13}	C_{33}	C_{44}	C_{66}	E_g^{HSE06}	ω_{po}
KCdAs	13.65/7.06	9.64/3.95	-3.49/-1.96	2.52/0.62	0.97/1.34	69.16	12.25	16.05	41.77	13.35	19.05	0.72	3.68

tive approach. Given the computationally expensive nature of iterative solving for 4ph processes, we employ the single-mode relaxation time approximation (SMRTA)[41] to handle 4ph scattering processes[42]. Finally, we define κ_L as follows:

$$\kappa_{\mathrm{L}}=\frac{\hbar^2}{\mathrm{k_B}T^2VN_q}\sum_{\lambda}n_\lambda\left(n_\lambda+1\right)\omega_\lambda^2\upsilon_\lambda F_\lambda, \tag{1}$$

where $\hbar$ is the reduced Planck's constant, $\mathrm{k_B}$ is the Boltzmann constant, T is the absolute temperature, V is unit cell volume, N_q is the total number of sampled phonon wave vectors in the first Brillouin zone, λ is the abbreviation of wave vector $\mathbf{q}$ and branch index ν, ω_λ is the frequency, and υ_λ is phonon group velocity. Besides, the F_λ is written as

$$F_\lambda=\tau_\lambda(\upsilon_\lambda+\Delta_\lambda), \tag{2}$$

in which τ_λ is the phonon lifetime of SMRTA, Δ_λ is the number of population deviations for the iterative solution.

For electronic transport parameters, we utilized the electronic Boltzmann transport equation and solved for them using the AMSET software package. By using Fermi's golden rule, the differential scattering rate of materials from initial state $\psi_{n\mathbf{k}}$ to final state $\psi_{m\mathbf{k+q}}$ can be written as

$$\tilde{\tau}^{-1}_{n\mathbf{k}\to m\mathbf{k+q}}=\frac{2\pi}{\hbar}|g_{nm}(\mathbf{k},\mathbf{q})|^2\delta(\varepsilon_{n\mathbf{k}}-\varepsilon_{m\mathbf{k+q}}), \tag{3}$$

in which n and m are the sign of the energy level, $\mathbf{k}$ and $\mathbf{k}$+$\mathbf{q}$ denote the coordinates of reciprocal space, $\varepsilon_{n\mathbf{k}}$ is the energy state $\psi_{n\mathbf{k}}$, and $g_{nm}(\mathbf{k},\mathbf{q})$ is the electron-phonon scattering matrix element from initial state $\psi_{n\mathbf{k}}$ into final state $\psi_{m\mathbf{k+q}}$. Finally, the rational carrier relaxation time can be calculated, the τ as

$$\frac{1}{\tau^{\mathrm{tot}}}=\mathrm{P^{ADP}}+\mathrm{P^{POP}}+\mathrm{P^{IMP}}, \tag{4}$$

are the scattering rates of the completely anisotropic acoustic deformation potential, the scattering rates of the polar optical phonon, and the scattering rates of ionized impurity, respectively, the results are shown in Supplementary Material Fig. S2[36]. The electron transport properties were computed by the generalized transport coefficients

$$L^n_{\alpha\beta}=e^2\int\Sigma_{\alpha\beta}(\varepsilon)\left(\varepsilon-\varepsilon_F\right)^n\left[-\frac{\partial f^0}{\partial\varepsilon}\right]d\varepsilon \tag{5}$$

In the provided equation, where α and β represent Cartesian coordinates, $\sum_{\alpha\beta}(\varepsilon)$ is the spectral conductivity, ε_F is the Fermi level at a specific doping concentration and temperature, and f^0 is the Fermi-Dirac distribution, the properties are derived as follows:

$$\sigma_{\alpha\beta}=e^2\int\Sigma_{\alpha\beta}(\varepsilon)[-\frac{\partial f^0}{\partial\varepsilon}]d\varepsilon, \tag{6}$$

$$S_{\alpha\beta}=\frac{1}{eT}\frac{\int\Sigma_{\alpha\beta}(\varepsilon)(\varepsilon-\varepsilon_F)[-\frac{\partial f^0}{\partial\varepsilon}]d\varepsilon}{\int\Sigma_{\alpha\beta}(\varepsilon)[-\frac{\partial f^0}{\partial\varepsilon}]d\varepsilon}, \tag{7}$$

$$\kappa_{\alpha\beta}=\frac{1}{T}\left\{\frac{\left(\int\Sigma_{\alpha\beta}(\varepsilon)(\varepsilon-\varepsilon_F)\left[-\frac{\partial f^0}{\partial\varepsilon}\right]d\varepsilon\right)^2}{\int\Sigma_{\alpha\beta}(\varepsilon)\left[-\frac{\partial f^0}{\partial\varepsilon}\right]d\varepsilon}-\int\Sigma_{\alpha\beta}(\varepsilon)(\epsilon-\varepsilon_F)^2\left[-\frac{\partial f^0}{\partial\varepsilon}\right]d\varepsilon\right\} \tag{8}$$

As previously elucidated, the essential material parameters, encompassing dielectric constant, elastic constants, effective phonon frequencies, band gap, and deformation potentials, have been determined through DFT calculations, as exemplified in Table 1.

III. RESULTS AND DISCUSSION

The ternary arsenide KCdAs crystallizes in an orthorhombic crystal system with a space group of P4/nmm [125]. We have visualized its unit cell structure using the VESTA[43] software, as shown in Figure 1. Table 2 lists the optimized lattice constants for KCdAs, which have been compared to experimental values. The errors for both the a(b)-axis and the c-axis are within 1%, indicating the reliability of our lattice optimization results. Phonons transmit energy through the vibrations of atoms in the lattice, facilitating the transfer of heat from one location to another. Therefore, we pay significant attention to the arrangement of atoms in the crystal lattice. In KCdAs, the non-equivalent layers of arsenic atoms encapsulate the cadmium atoms in the center. The non-isovalent As atom and the Cd atom embedded in its core form a tetrahedral structure. These tetrahedra intricately interweave, composing a stratified architecture extending along the a(b)-axis. Meanwhile, the K atomic layers are arranged between the tetrahedral layers.

TABLE II. The calculations encompassed the determination of the lattice parameters (a(b)/c^{opt} ($\AA$)), the bulk modulus (B), shear modulus (G_{VRH}), Young's modulus (E), Pugh's ratio (B_H/G_H), Poisson's ratio (ν), universal anisotropic index (A^U), the percent anisotropic of shear modulus (A_G), and Debye temperature (θ_D) for KCdAs. The experimental lattice parameters (a(b)/c^{expt})[22] were also listed for comparison.

semiconductor	a(b)^{opt}	a(b)^{expt}	c^{opt}	c^{expt}	B	G_V	G_R	G_H	E	B_H/G_H	ν	A^U	A_G	θ_D
KCdAs	4.52	4.55	7.90	7.98	29.25	18.20	16.69	17.45	43.66	1.68	0.25	0.49	0.04328	213.50

In Table 1, the elastic constants of the material have been computed. Apart from serving as input parameters for AMSET, they also find utility in assessing the mechanical stability of the material. The criteria for mechanical stability can be articulated as follows:

$$\begin{aligned} C_{11} > |C_{12}|, \qquad & C_{44} > 0, \\ 2C_{13}^2 < C_{33}(C_{11}+C_{12}), \qquad & C_{66} > 0. \end{aligned} \tag{6}$$

The computed results satisfying the aforementioned criteria confirm that KCdAs exhibits mechanical stability. Furthermore, employing the Voigt-Reuss-Hill method[44–46], the mechanical properties of the ternary arsenide have been thoroughly investigated. The outcomes are presented in Table 2, providing the volumetric modulus (B), shear modulus (G), and Young's modulus (E) for KCdAs[47–49]. We have also determined that KCdAs is a brittle material based on both Pugh's ratio (<1.75) and Poisson's ratio (<0.26). Mechanical anisotropy is a key strategy in enhancing the material's durability. In this study, the universal anisotropic index A^U and percent anisotropic of shear modulus A_G are used to measure anisotropy (deviation from 0). The calculated results indicate that both A^U and A_G exhibit relatively high values, signifying that KCdAs possesses pronounced mechanical anisotropy.

Traditional solutions based on the HA for the BTE often lead to imaginary phonon frequencies when calculating the phonon dispersions of most stable materials. This is evidently an unreasonable outcome. Therefore, we employ a self-consistent phonon theory that accounts for high-order anharmonic effects in the lattice to compute the anharmonic phonon frequencies at finite temperatures. As depicted in Figure 2(a), we have computed the temperature-dependent phonon dispersion curve. It is evident that the entire phonon spectrum displays a hardening phenomenon, with the high-order anharmonic effects on the acoustic phonon branch significantly trailing those on the optical phonon branch. Subsequently, we conducted calculations for the anharmonic phonon density of states (AHPDOS) at 300 K, as illustrated in figures 2(b). This figure reveal that the primary contribution to the low-frequency phonon branch emanates from the heavier Cd and As atoms. Interestingly, the predominant contribution to the high-frequency optical phonon branch is also attributed to the As and Cd atoms. In general, the lower-frequency phonon branch is occupied by atoms with greater atomic mass, whereas the higher-frequency phonon branch is inhabited by atoms with lighter atomic mass. Moving forward, we initiated an investigation into the anomaly of heavier Cd and As atoms inhabiting the high-frequency phonon branches. At the Γ point, under the HA, we calculated the vibrational modes of the phonon branches corresponding to the state density peaks of As and Cd atoms at high frequencies. We then correlated their vibration directions and magnitudes with their respective atoms, as depicted by the arrows in Figure 1. Figures 1(a) and (b) represent the vibration modes corresponding to the As atomic peak and the Cd atomic peak, respectively. We observed that in Figure 1(a), the As atomic peak primarily arises from the relative vibrations of non-equivalent As atoms along the a(b)-axis. In contrast, the Cd peak in Figure 1(b) is a result of As atoms vibrating collectively along the c-axis direction, driving the central Cd atom into simultaneous motion. However, due to the greater atomic mass of Cd compared to As, Cd and As atoms may exhibit a substantial phase difference along the c-axis. To validate the aforementioned hypothesis, we proceeded to calculate the atomic mean square displacement (MSD) of KCdAs and the integrated partial of the crystal orbital Hamilto-

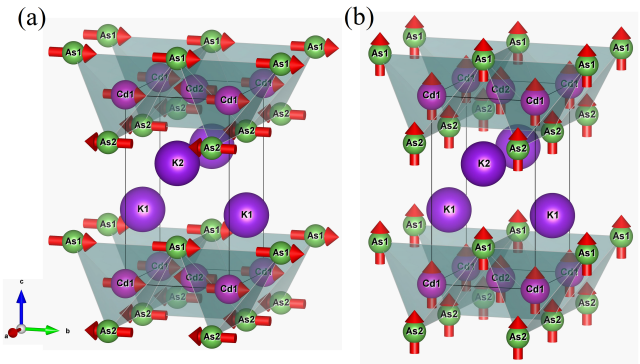

FIG. 1. (Color online). We visualized the crystal structure of KCdAS through VESTA software. K, Cd, and As atoms are represented by purple, pink, and green balls respectively. The As1 and As2 layers wrap Cd atoms into a tetrahedral structure, and K atoms are isolated between the tetrahedrons. The arrows of atoms in (a) and (b) respectively represent the vibration modes of the corresponding density of states peaks of As and Cd atoms at high frequencies at the Γ point. The vibrations of K atoms are too weak, so they are not shown.

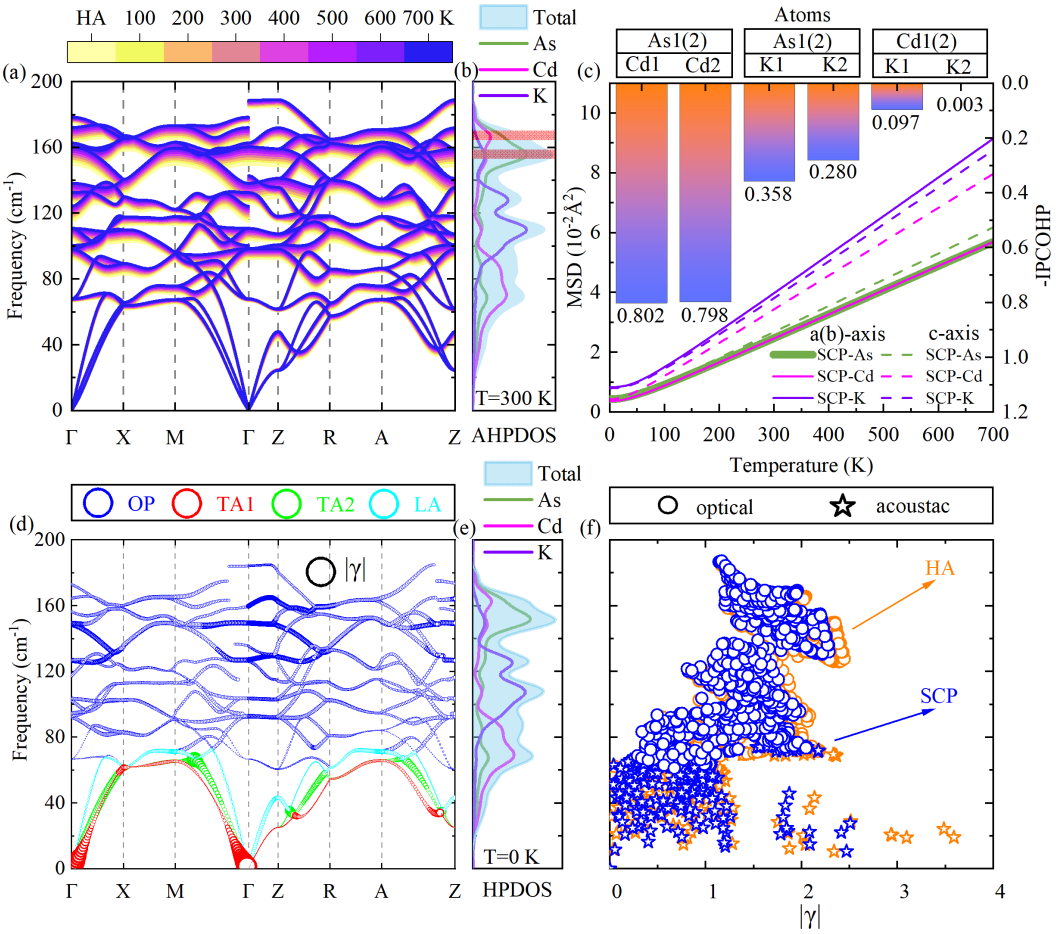

FIG. 2. (Color online). (a) Represents the phonon spectrum at 0 ∼ 700 K under the HA and SCP approximations, which we use gradient colors from yellow to purple to blue. (b) Represents the projected density of states of atoms at 300 K. (c) Changes of different atoms with temperature along the a(b)- and c-axes, and the integrated partial of the crystal orbital Hamiltonian population (IPCOHP) between different atoms. (d) Bubble diagram of the Grüneisen parameter (γ) projected onto the HA phonon spectrum, with the acoustic phonon branch and the optical phonon branch distinguished by different colors. (e) Represents the projected state density of atoms under the HA approximation. (f) We use orange and blue to represent the magnitude of the γ at different phonon frequencies under the HA and SCP approximations, respectively, and use five-pointed stars and circles to distinguish the acoustic phonon branch and the optical phonon branch.

nian population (IPCOHP) at the Fermi level, as shown in Figure 1(c). It is worth noting that As and Cd atoms maintain the same size MSD in the a(b)-axis direction (we show it with lines of different thicknesses). This is because As and Cd atoms exhibit bonding states and interact with other atoms. There is a stronger interaction between them. At the same time, the weak interaction between K atoms and surrounding atoms and the large MSD indicate that K atoms are weakly bound in the unit cell. The Cd atom shows strong anisotropy, and the difference between its a(b)-axis and c-axis MSD is much larger than that of As and K atoms, which is consistent with the above analysis.

Generally speaking, a larger MSD value means a shallower potential energy surface, that is, a lower force constant and a weakly bonded atom[50]. Therefore, larger MSDs or shallow electrical potential wells can identify significant rattling behavior. As shown in Figure 3, in KCdAs, Cd atoms have a shallow potential energy well along the a(b)-axis. This is due to the strong bonding of Cd and As atoms forming a tetrahedral layer in the a(b)-axis, the non-equivalent As atoms drag the heavier Cd atoms, causing the Cd atoms to have greater anharmonicity along the a(b)-axis in the tetrahedral layer. Similarly, the potential energy surface of K atoms in the c-axis direction is lower than that of other atoms. This is due to the fact that the K atomic layer is located between the Cd-As tetrahedral layers, and its weak bonding and large MSD show obvious rattling behavior. Therefore, K atoms also have strong anharmonicity on the c-axis.

In our analysis, we have not taken into account the complete non-harmonic phonon frequency shift. From the perspective of phonon self-energy, the quartic anharmonicity induces a first-order correction to the phonon

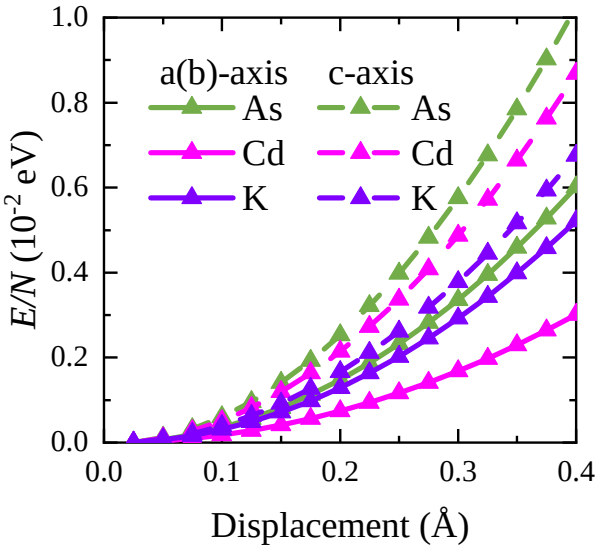

FIG. 3. (Color online). We calculated potential energy curves for all atoms of KCdAs as a function of displacement around the equilibrium position along the a(b)- and c-axis directions.

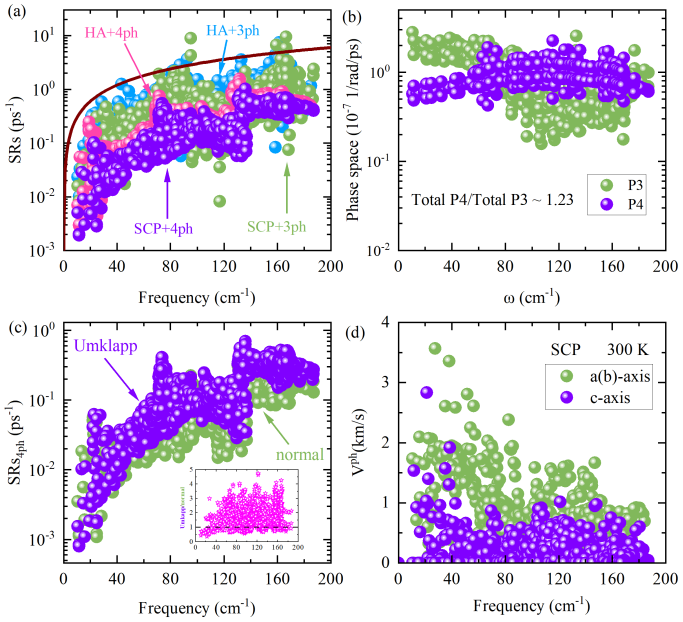

FIG. 4. (Color online). (a) The scattering rate of 3ph and 4ph is obtained based on the approximation of HA+3,4ph and SCP+3,4ph, represented by blue, pink, green, and purple, respectively. The quasiparticle line is given, represented by a wine-red curve. (b) The 3ph and 4ph scattering phase space and the overall P4 to P3 ratio. (c) We decompose the scattering rate of SCP+4ph into U and n processes and draw a scatter plot comparing the U/n ratio with 1. (d) Group velocities along different directional axes at 300 K under the SCP approximation are plotted.

energy, whereas the cubic anharmonicity primarily governs the second-order correction. The SCP theory exclusively deals with the first-order correction and thus neglects the phonon frequency shift caused by cubic nonharmonicity[30]. However, this should not be misconstrued as implying that the quartic anharmonicity is more influential than the cubic anharmonicity. The real part of the self-energy predominantly governs the phonon frequency shift, while the imaginary part manifests in alterations to the phonon scattering rate. Generally, it is the cubic anharmonic effect that results in a more significant impact on phonon interactions compared to the quartic anharmonicity.

Next, we will conduct a specific analysis of the results obtained by taking into account the cubic and quartic anharmonic effects. In Figure 2(d), we represent the computed Grüneisen parameter (γ) as a bubble diagram projected onto the HA phonon spectrum. The response from Γ to Z corresponds to γ along the c-axis direction, while the sizes of the bubbles, excluding this, represent γ along the a(b)-axis direction. Figure 2(e) displays the harmonic phonon density of states (HPDOS) under the HA approximation. The γ is derived as the partial derivative of the cubic potential energy expansion with respect to the quadratic potential energy expansion, offering insight into the material's cubic anharmonicity strength. The data reveals that the predominant manifestation of cubic anharmonicity within KCdAs is confined to the low-frequency acoustic phonon branch, i.e the transverse acoustic phonon branch (TA). Furthermore, it is evident that the γ component along the a(b)-axis significantly surpasses that along the c-axis, underscoring the substantial anharmonicity characterizing the a(b)-axis, which aligns seamlessly with the observation that the potential energy surface along the a(b)-axis, as depicted in Figure 2, is of lesser extent in comparison to the c-axis. Additionally, our observations have unveiled a distinct coupling between the longitudinal acoustic (LA) phonon branch and the low-frequency optical phonon branch. This acoustic-optical coupling means that the probability of collision and scattering between the acoustic phonon branch and the optical phonon branch is greatly increased, which will reduce κ_L has a promoting effect. Different from cubic anharmonicity, the renormalization of the phonon spectrum reflects the correction of the real part of the phonon self-energy by the quartic anharmonicity. The acoustic phonon branch is almost unaffected, while the optical phonon branch shows great hardening, and the phonon group speed will also be significantly increased, which will be beneficial to heat transfer. When we compare the γ of HA and SCP approximately at 300 K, we will find that the γ of SCP is lower than that of HA. This is because the quartic anharmonicity renormalization of the phonon frequency suppresses the γ, as shown in Figure 2(f).

In addition, higher-order anharmonicity also plays a crucial role in the imaginary part of phonon self-energy. Therefore, we studied the impact of cubic and quartic anharmonicity on τ_{ph}, as shown in Figure 4(a). In order to verify the effectiveness of the phonon quasiparticle image,

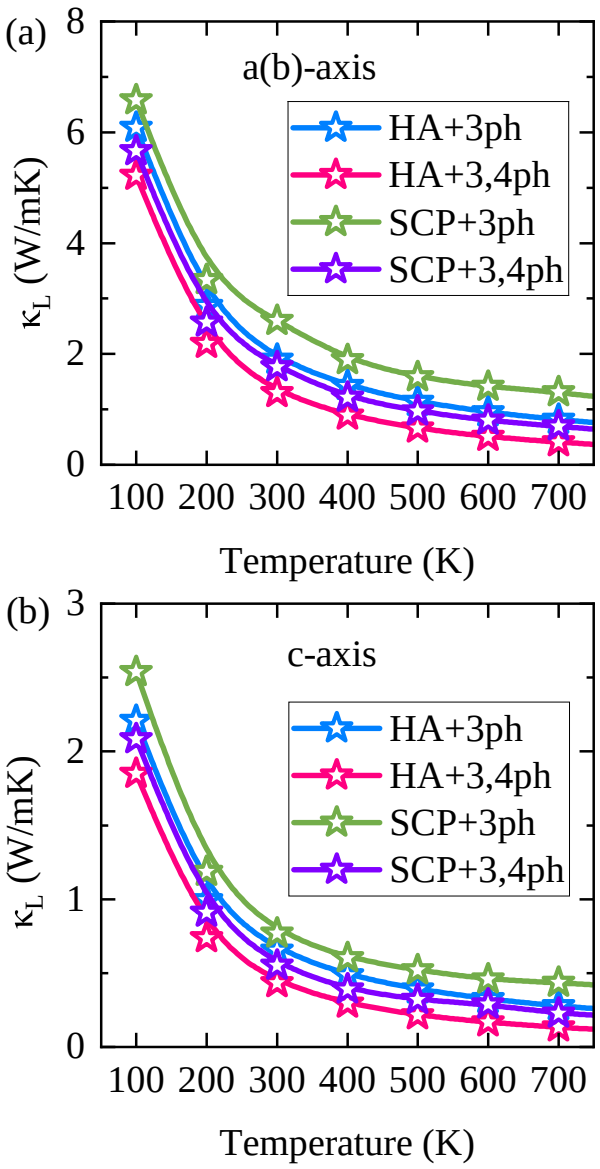

FIG. 5. (Color online). (a) and (b) present the temperature-dependent variations of κ_L along the a(b)-axis and c-axis under four approximations: HA+3ph, HA+3,4ph, SCP+3ph, and SCP+3,4ph.

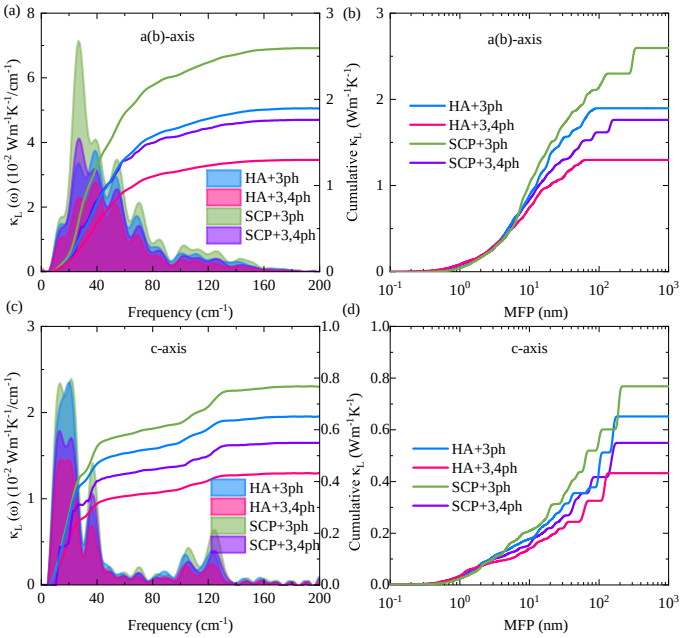

FIG. 6. (Color online). (a) and (c) represent the lattice thermal conductivity spectra $\kappa_L(\omega)$ (filled area below the curves) and relevant cumulative κ_L (in lines) in KCdAs at 300 K on the a(b)- and c-axes, respectively. (b) and (d) represent the functions of phonon mean free paths (MPMFPs) at 300 K for the a(b)- and c-axes, respectively. We use blue, pink, green, and purple to represent the HA+3ph, HA+3,4ph, SCP+3ph, and SCP+3,4ph approximations, respectively.

we also use a burgundy line to represent $1/\tau=\omega/2\pi$ in Figure 4(a). The part beyond the quasiparticle line indicates that the wave packet of the phonon is larger than its vibration period, that is, the phonons overlap. We think that the phonon is annihilated before completing a vibration cycle. At this time, the phonon in the quasi-particle image is invalid. The 3ph and 4ph scattering rates we calculated are almost all distributed below the $1/\tau=\omega/2\pi$ curve, which confirms the effectiveness of phonon BTE. We found that the large 3ph and 4ph SRs are one of the main reasons for the ultralow lattice thermal conductivity of KCdAs. It is worth noting that in the low-frequency phonon mode within the effective quasiparticle image, 4ph scattering is of the same order of magnitude as 3ph scattering, which indicates that 4ph scattering also plays an important role in the heat transport process. The 3ph scattering rate is jointly determined by the 3ph scattering phase space (W_{3ph}) and γ. W_{3ph} represents the number of 3ph scattering channels, and γ represents the scattering intensity of 3ph. We decompose 3ph SRs and W_{3ph} into two independent processes in Supplementary Material Fig. S3[36], including splitting ($\lambda \rightarrow \lambda'+\lambda''$) and combination ($\lambda+\lambda' \rightarrow \lambda''$) process. In order to satisfy the conservation of energy and momentum, low-frequency phonon modes tend to combine into high-frequency phonon modes, while high-frequency phonon modes tend to split into low-frequency phonon modes. At the same time, the W_{3ph} is strictly constrained by selection rules, resulting in strong 4ph SRs. We also decompose 4ph SRs and 4ph scattering phase space (W_{4ph}) into three independent processes, including splitting ($\lambda \rightarrow \lambda'+\lambda''+\lambda'''$), recombination ($\lambda+\lambda'+\lambda'' \rightarrow \lambda'''$) and redistribution ($\lambda+\lambda' \rightarrow \lambda''+\lambda'''$) process, as shown in Figure. S4 in the supplementary material[36]. The above rules are also applicable to 4ph SRs. It is worth noting that the redistribution process is more flexible in meeting the conditions required for phonon energy, so it accounts for the main contribution. Under 300 K, the total scattered phase space of 4ph is even greater than the total scattering phase space of 3ph, as shown in Figure 4 (b),

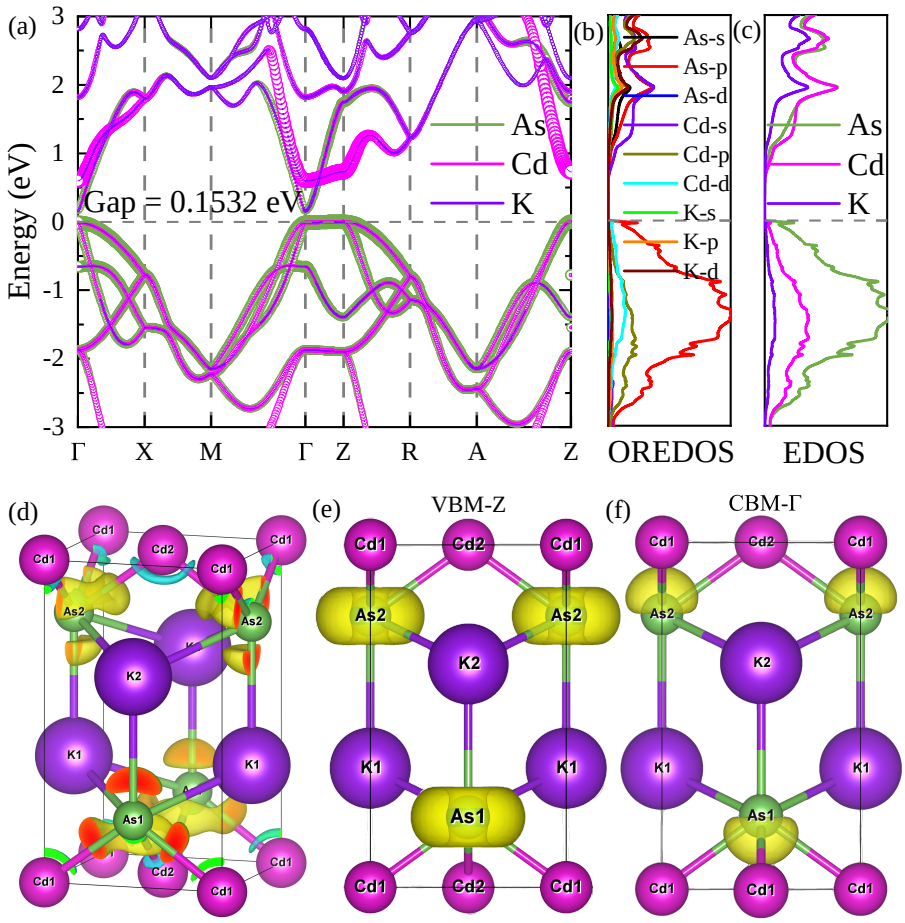

FIG. 7. (Color online). (a), (b) and (c) Use PBE functional to calculate the projected electronic band structure, orbital electron band density of states (OREDOS) and corresponding electron projected density of states (EDOS) of KCdAs. We will Fermi The energy level is set to 0 eV. (d) is the calculated differential charge density. (e) and (f) calculate the partial electron density at the top and bottom of the valence band, respectively.

which means that 4ph has more number of scattering channels, and 4ph and 3ph scattering are in the same number of magnitude magnitude magnitudes Therefore, 4ph also has a strong scattering strength. The decomposed anharmonic (3ph and 4ph) scattering phase spaces exhibit similar patterns to the decomposed anharmonic scattering rates.

In addition, we also expressed the 4ph process in the Umklapp and normal processes. As shown in Figure 4 (c), the normal process does not generate heat resistance directly, but the momentum between the dynamics is reorganized. The process provides thermal resistance and hinders the movement of the phonons. We can see that the Umklapp process is generally larger than the normal process (see the ratio of Umklapp/normal in Figure 4 (c)). Therefore, the 4ph scattering process is mainly due to the reduction of κ_L due to heat resistance. Then, when we compared 300 K in Figure 4 (d), the SCP is similar to the difference between the speed of the a-(b) axis and the c-axis group. Consistent with previous analysis, the group speed of the c-axis is far less than the a-(b) axis, so it is predicted that the κ_L will be lower than the a-(b) axis.

Finally, we computed the temperature-dependent curves of κ_L along the a(b)-axis and c-axis using four different methods (HA+3ph, HA+3,4ph, SCP+3ph, and SCP+3,4ph), As shown in Figure 5. At 300 K, the κ_L values obtained by SCP+3,4ph are approximately 1.76 and 0.55 (W/mK) along the a(b)-axis and c-axis, respectively, reaching the same level as those exhibited by classical thermoelectric materials. According to the Debye law, the specific heat capacity reaches a steady state at high temperatures (see Supplementary Material Figure. S5[36]), and the system's κ_L is primarily determined by τ and υ. As indicated by the formulation (4) in the methods and Figure 4(a), the smaller SRs component (acoustic phonon branch) occupies a larger proportion in heat transfer. This is attributed to the requirement for phonons to satisfy the Einstein distribution function, making it difficult to excite high-frequency phonons. Consequently, the low-frequency acoustic branch makes the predominant contribution to heat transport, as de-

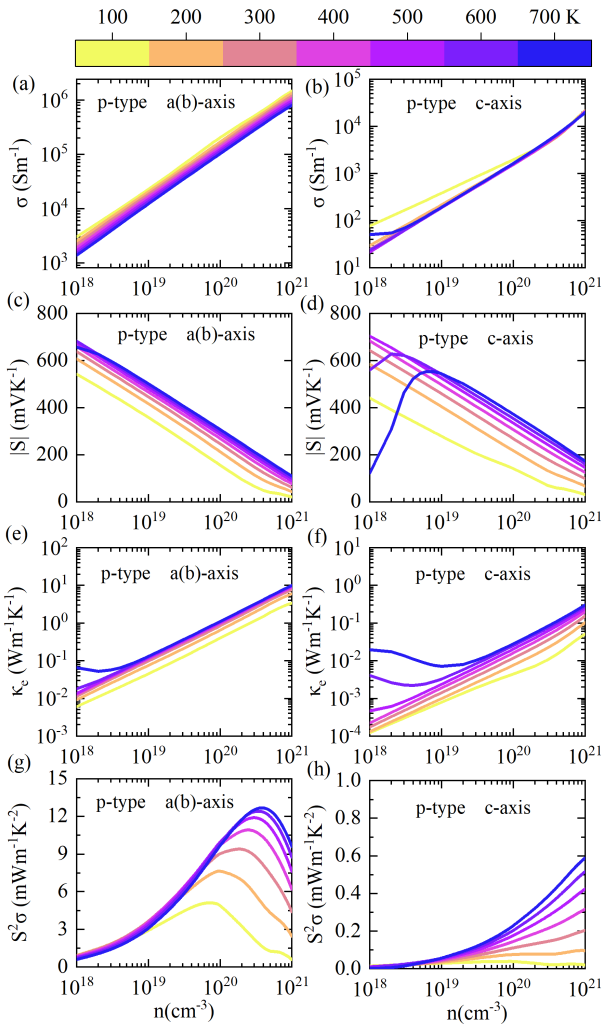

FIG. 8. (Color online). The absolute value of the Seebeck coefficient $|S|$, the electrical conductivity σ, the power factor $S^2\sigma$ and the thermal conductivity of KCdAs under p-type doping were calculated Coefficient κ_e. The left columns (a), (c), (e), and (g) represent the a (b)-axis, and the right columns (b), (d), (f), and (h) represent the c-axis. The color gradient from yellow to violet to blue represents the temperature dependence from 100 K to 700 K.

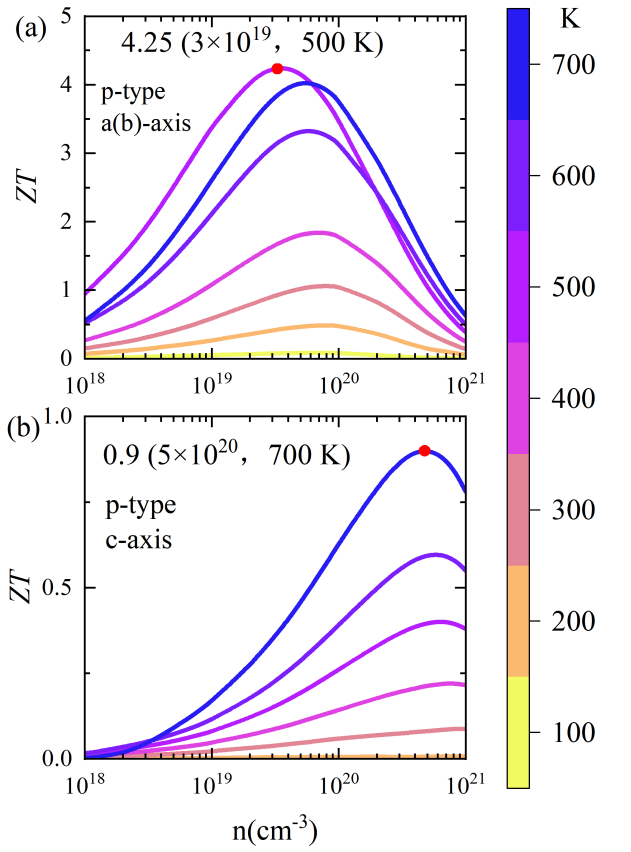

FIG. 9. (Color online). (a) and (b) We calculated the TE figure of merit along the a-(b) axis and (c)-axis of KCdAs under p-type doping at 0∼700 K.

picted in Figures 6(a) and (c). As discussed earlier, the analysis suggests that the acousto-optic coupling primarily occurs along the a(b)-axis direction, indicating that τ along the a(b)-axis is smaller than that along the c-axis. Furthermore, v along the a(b)-axis is significantly greater than that along the c-axis. The sizes of κ_L along the a(b)-axis and c-axis are in agreement with the v. In other words, the v plays a decisive role in determining the directional dependence of κ_L. Figures 6(b) and (c) depict the cumulative κ_L as a function of the maximum Mean Free Path (MFP). The outcomes indicate that heat-carrying phonons possess relatively large MFPs at 300 K. We can mitigate $\kappa^{\mathrm{SCP}}_{3,4ph}$ through nanostructuring, for instance, restricting the maximum MFP to 10 nm yields values as low as 0.83 and 0.156 $\mathrm{WK^{-1}m^{-1}}$ along the a(b)- and c-axis, respectively.

Next, we will focus on the analysis of the electronic transport properties of KCdAs. Based on the PBE exchange-correction function, the band gap of KCdAs is determined to be 0.1532 eV. However, the PBE exchange-correction function significantly underestimates the band gaps of semiconductors. Therefore, we utilize the band gap of 0.7156 eV obtained with the HSE06[51] exchange-correction function, with a scissor correction applied to align the gap values (see Supplementary Material Figure. S6[36]). Since there are no significant differences in the electronic band structures between calculations using the HSE06 and PBE functionals, apart from the band gap, we employ the PBE calculated electronic band structure, orbital-resolved electronic density of states (ORE-DOS), and total electronic density of states (EDOS) to qualitatively study the electronic transport properties of these two materials, as shown in Figures 7(a), (b), and (c). KCdAs is an indirect band gap semiconductor, with the valence band maximum (VBM) and conduction band minimum (CBM) located at the Z and Γ high-symmetry points, respectively. The CBM is primarily contributed by the p orbitals of As and the s orbital of Cd, while the VBM is predominantly shaped by the p orbitals of As.

The CBM exhibits high electron band dispersion, indicative of a high σ. Furthermore, along the Γ to Z direction, there is a nearly flat band near the energy of the next valence band maximum. This implies that along the c-axis, under n-type doping, there is a significant $|S|$, leading to a large PF. However, although the VBM exhibits a very flat band along the Γ to Z direction, it sacrifices its dispersion. Therefore, the σ along the c-axis is expected to be small, resulting in a relatively modest PF. It is noteworthy that along the Γ to X direction, there is a coexistence of a large flat band and high dispersion in the VBM. This suggests that both σ and $|S|$ have significant values, leading to the capture of a large PF. Figure 7(d) provides the differential charge density map of KCdAs, with yellow and cyan indicating electron accumulation and depletion, respectively. The figure reveals that Cd atoms lose electrons, forming an electron cloud around As atoms. Consequently, there is a strong bonding between As and Cd atoms, consistent with the results of the IPCOHP analysis. In addition, we also gave the VBM and CBM partial electron density, as shown in Figure 7 (e) and (f), which also verified our speculation of different axes, p- and n-type σ.

Therefore, we calculated the electronic transport parameters for KCdAs, as shown in Figure 8 (p-type) and Supplementary Material Figure. S7 (n-type)[36]. Just as analyzed in our examination of the electronic band dispersion, for p-type doping, σ along the a(b)-axis is higher than that along the c-axis, and both maintain relatively high $|S|$. On the other hand, for n-type doping, despite having higher σ, the $|S|$ is much lower than for p-type. Therefore, the coexistence of large $|S|$ and σ allows KCdAs to exhibit superior PF in the a(b)-axis direction under p-type doping. Additionally, we observe that σ is proportional to the carrier concentration (n) and inversely proportional to the T. The former is due to an increase in the number of carriers participating in the conduction process with the increase in n. The latter is attributed to an increase in the scattering rate caused by the electron-phonon interaction as the temperature rises, consistent with the results shown in Supplementary Material Figure. S2. Unlike σ, at the same T, $|S|$ decreases with increasing n, and at the same n, $|S|$ increases with increasing T. The variation of κ_e with n follows the same trend as σ. It is noteworthy that due to the double peak effect, for p-type doping, $|S|$ along the c-axis exhibits a single peak at 600 K and 700 K[52]. This phenomenon has been observed in materials with narrow band gaps[53, 54]. While there is no appearance of a single peak for $|S|$ along the a(b)-axis under p-type doping, the strong double peak effect still inhibits $|S|$, and it increases with temperature. Therefore, at low n, the PF values captured at 500 K are larger. Furthermore, we have solely employed the BTE to estimate the electronic transport characteristics under specific doping concentrations, without considering specific p-type and n-type doping. We look forward to future research by scientists for further experimental and theoretical exploration of this material.

Finally, in KCdAs, the combination of low κ_L and high PF results in an exceptionally high ZT of ∼4.25 along the a(b)-axis at $n_h \sim 3\times10^{19}$ and 500 K. However, along the c-axis, the ZT is 0.90 at the optimal n and T, as shown in Figure 9. n-type doping at 700 K also exhibits excellent thermoelectric performance, especially along the c-axis. Despite having a lower PF compared to p-type, the ultra-low κ_L along the c-axis results in a ZT value of 2.36 at n_e of 1×10^{18} at 700 K, as illustrated in Supplementary Material Figure. S8[36].

IV. CONCLUSION

In summary, this paper employs advanced first-principles methodology, integrating SCP and the BTE, to comprehensively investigate the thermal transport and thermoelectric properties of KCdAs. The study meticulously considers the renormalization of υ due to finite-temperature phonon frequencies induced by quartic anharmonicity in the pursuit of κ_L. Additionally, the paper explores the impacts of 3ph and 4ph scattering processes on τ. Through various methodologies, including examining atomic vibrational modes, phonon spectra, γ, atomic mean-square displacements, and analyses of 3ph and 4ph scattering processes, the study reveals intricate microphysical mechanisms contributing to the observed low κ_L within KCdAs. The notable features of KCdAs include significant anisotropy in Cd atoms, pronounced anharmonicity in K atoms, and relative vibrations in non-equivalent As atomic layers, all contributing to high vibrational frequencies for As atoms. Additionally, Cd atoms, situated between As atomic layers, exhibit rattling modes and strong lattice anharmonicity, contributing to the low κ_L within KCdAs. Remarkably flat bands and favorable dispersion near the valence band maximum indicate superior electronic properties, resulting in high power factors (PF). The coexistence of ultra-low κ_L and high PF aligns with the pursuit of exceptional thermoelectric performance. Under optimal temperature and carrier concentration doping in both p-type and n-type regions, the study achieves outstanding ZT values of 4.25 (a(b)-axis, p-type), 0.90 (c-axis, p-type), 1.78 (a(b)-axis, n-type), and 2.36 (c-axis, n-type).

Acknowledgment

This research were supported by the Natural Science Foundation of Shandong Province for Major Basic Research under Grant No.ZR2023ZD09, the National Natural Science Foundation of China under Grant No.12174327, No.11974302 and No.92270104.

Declaration of competing interest

The authors declare no conflict of interest.

[1] L. E. Bell, Science **321**, 1457 (2008).
[2] G. J. Snyder and E. S. Toberer, Nature materials **7**, 105 (2008).
[3] J. Sootsman, D. Chung, and M. Kanatzidis, Angewandte Chemie International Edition **48**, 8616 (2009).
[4] M. Zebarjadi, K. Esfarjani, M. Dresselhaus, Z. Ren, and G. Chen, Energy & Environmental Science **5**, 5147 (2012).
[5] D. G. Cahill, S. K. Watson, and R. O. Pohl, Phys. Rev. B **46**, 6131 (1992).
[6] D. T. Morelli, V. Jovovic, and J. P. Heremans, Phys. Rev. Lett. **101**, 035901 (2008).
[7] G. P. Meisner, D. T. Morelli, S. Hu, J. Yang, and C. Uher, Phys. Rev. Lett. **80**, 3551 (1998).
[8] J. L. Cohn, G. S. Nolas, V. Fessatidis, T. H. Metcalf, and G. A. Slack, Phys. Rev. Lett. **82**, 779 (1999).
[9] L. D. Hicks and M. S. Dresselhaus, Phys. Rev. B **47**, 12727 (1993).
[10] D. Parker, X. Chen, and D. J. Singh, Phys. Rev. Lett. **110**, 146601 (2013).
[11] D. I. Bilc, G. Hautier, D. Waroquiers, G.-M. Rignanese, and P. Ghosez, Phys. Rev. Lett. **114**, 136601 (2015).
[12] H. Wu, L.-D. Zhao, F. Zheng, D. Wu, Y. Pei, X. Tong, M. Kanatzidis, and J. He, Nature communications **5**, 4515 (2014).
[13] T. Tadano, Y. Gohda, and S. Tsuneyuki, Phys. Rev. Lett. **114**, 095501 (2015).
[14] G. S. Nolas, J. Poon, and M. Kanatzidis, MRS bulletin **31**, 199 (2006).
[15] G. J. Snyder, M. Christensen, E. Nishibori, T. Caillat, and B. B. Iversen, Nature materials **3**, 458 (2004).
[16] L. Bjerg, B. B. Iversen, and G. K. H. Madsen, Phys. Rev. B **89**, 024304 (2014).
[17] X. Lu, D. T. Morelli, Y. Xia, F. Zhou, V. Ozolins, H. Chi, X. Zhou, and C. Uher, Advanced Energy Materials **3**, 342 (2013).
[18] L.-D. Zhao, S.-H. Lo, Y. Zhang, H. Sun, G. Tan, C. Uher, C. Wolverton, V. P. Dravid, and M. G. Kanatzidis, nature **508**, 373 (2014).
[19] C. W. Li, J. Hong, A. F. May, D. Bansal, S. Chi, T. Hong, G. Ehlers, and O. Delaire, Nature Physics **11**, 1063 (2015).
[20] W. Liu, X. Tan, K. Yin, H. Liu, X. Tang, J. Shi, Q. Zhang, and C. Uher, Phys. Rev. Lett. **108**, 166601 (2012).
[21] Y. Zhang, J.-H. Bahk, J. Lee, C. S. Birkel, M. L. Snedaker, D. Liu, H. Zeng, M. Moskovits, A. Shakouri, and G. D. Stucky, Advanced Materials **26**, 2755 (2014).
[22] H. Kahlert and H. Schuster, Z. Naturforsch., b;(Germany, Federal Republic of) **31** (1976).
[23] G. Tan, F. Shi, S. Hao, L.-D. Zhao, H. Chi, X. Zhang, C. Uher, C. Wolverton, V. P. Dravid, and M. G. Kanatzidis, Nature communications **7**, 12167 (2016).
[24] Y. Zhao, C. Lian, S. Zeng, Z. Dai, S. Meng, and J. Ni, Phys. Rev. B **101**, 184303 (2020).
[25] L.-C. Yin, W.-D. Liu, M. Li, Q. Sun, H. Gao, D.-Z. Wang, H. Wu, Y.-F. Wang, X.-L. Shi, Q. Liu, and Z.-G. Chen, Advanced Energy Materials **11**, 2102913 (2021).
[26] N. R. Werthamer, Phys. Rev. B **1**, 572 (1970).
[27] Y. Zhao, S. Zeng, G. Li, C. Lian, Z. Dai, S. Meng, and J. Ni, Phys. Rev. B **104**, 224304 (2021).
[28] G. Kresse and D. Joubert, Phys. Rev. B **59**, 1758 (1999).
[29] P. Hohenberg and W. Kohn, Phys. Rev. **136**, B864 (1964).
[30] T. Tadano and S. Tsuneyuki, Phys. Rev. B **92**, 054301 (2015).
[31] A. M. Ganose, J. Park, A. Faghaninia, R. Woods-Robinson, K. A. Persson, and A. Jain, Nature communications **12**, 2222 (2021).
[32] G. Kresse and J. Furthmüller, Computational Materials Science **6**, 15 (1996).
[33] G. Kresse and J. Furthmüller, Phys. Rev. B **54**, 11169 (1996).
[34] T. Tadano, Y. Gohda, and S. Tsuneyuki, Journal of Physics: Condensed Matter **26**, 225402 (2014).
[35] S. Baroni, S. de Gironcoli, A. Dal Corso, and P. Giannozzi, Rev. Mod. Phys. **73**, 515 (2001).
[36] *See Supplemental Material: for the methodology, phonon dispersion, thermodynamic stability testing, scattering rate, scattering phase spaces,energy band, electron conductivity, and TE values for KCdAs.*
[37] K. Esfarjani and H. T. Stokes, Phys. Rev. B **77**, 144112 (2008).
[38] F. Zhou, B. Sadigh, D. Åberg, Y. Xia, and V. Ozoliņš, Phys. Rev. B **100**, 184309 (2019).
[39] T. Feng, L. Lindsay, and X. Ruan, Phys. Rev. B **96**, 161201 (2017).
[40] T. Feng and X. Ruan, Phys. Rev. B **93**, 045202 (2016).
[41] A. J. H. McGaughey and M. Kaviany, Phys. Rev. B **69**, 094303 (2004).
[42] Z. Han, X. Yang, W. Li, T. Feng, and X. Ruan, Computer Physics Communications **270**, 108179 (2022).
[43] K. Momma and F. Izumi, Journal of Applied Crystallography **41**, 653 (2008).
[44] W. Chung, D.H.and Buessem, Journal of Applied Physics **38**, 2535 (2004).
[45] A. Reuss, ZAMM - Journal of Applied Mathematics and Mechanics / Zeitschrift für Angewandte Mathematik und Mechanik **9**, 49 (1929).
[46] R. Hill, Proceedings of the Physical Society. Section A **65**, 349 (1952).
[47] S. I. Ranganathan and M. Ostoja-Starzewski, Phys. Rev. Lett. **101**, 055504 (2008).
[48] P. Ravindran, L. Fast, P. A. Korzhavyi, B. Johansson, J. Wills, and O. Eriksson, Journal of Applied Physics **84**, 4891 (1998).
[49] Y. Tian, B. Xu, and Z. Zhao, International Journal of Refractory Metals and Hard Materials **33**, 93 (2012).
[50] W. Qiu, L. Wu, X. Ke, J. Yang, and W. Zhang, Scientific Reports **5** (2015).
[51] R. Pela, M. Marques, and L. Teles, Journal of Physics: Condensed Matter **27**, 505502 (2015).
[52] J. Gong, A. Hong, J. Shuai, L. Li, Z. Yan, Z. Ren, and J.-M. Liu, Physical chemistry chemical physics **18**, 16566 (2016).
[53] Y.-L. Pei and Y. Liu, Journal of Alloys and Compounds **514**, 40 (2012).
[54] H. Wang, Y. Pei, A. D. LaLonde, and G. J. Snyder, Advanced Materials **23**, 1366 (2011).